Sign reversal of unidirectional magnetoresistance in monocrystalline Fe/Pt bilayers

Xiang Zhou [1,2] Fanlong Zeng,[1] Mengwen Jia,[1] Haoran Chen,[1] and Yizheng Wu [1,3,*]

[1]*Department of Physics, State Key Laboratory of Surface Physics, Fudan University, Shanghai 200433, China*

[2]*ShanghaiTech Laboratory for Topological Physics & School of Physical Science and Technology, ShanghaiTech University, Shanghai 201210, China*

[3]*Shanghai Research Center for Quantum Sciences, Shanghai 201315, China*

(Received 17 August 2021; revised 29 October 2021; accepted 1 November 2021; published 8 November 2021)

The discovery of unidirectional magnetoresistance (UMR) in ferromagnet/heavy metal heterostructures provides one possibility to detect the magnetization direction with a simple two-terminal geometry. We investigated the temperature and thickness dependence of UMR in single-crystalline Fe/Pt bilayers and discovered an obvious sign reversal when increasing the Fe thickness at low temperature. Meanwhile, the same phenomenon is observed when increasing temperature for thick Fe samples. All the UMR mechanisms are quantitatively analyzed and the UMR contribution induced by the thermal effect shows a thickness-dependent sign change, thus the sign reversal of UMR is attributed to the competition between the contributions on UMR from the thermal effect and the spin accumulation induced by the spin Hall effect in the Pt layer. Our results emphasize the thermal contribution to the UMR in ferromagnet/heavy metal heterostructures and suggest a promising way to tune the UMR, which will promote its application in information storage devices.

DOI: 10.1103/PhysRevB.104.184413

I. INTRODUCTION

The heterostructures composed of a ferromagnet (FM) and heavy metal (HM) have become intriguing in recent decades due to the potential application in information storage devices and the abundant physical phenomena inside [1–5,5–14], such as spin pumping (SP) [6,8], spin Seebeck effect (SSE) [9,10], spin-orbit torque (SOT) [2,3], spin Hall magnetoresistance (SMR) [5,13,14], and so on. In the FM/HM heterostructures, it is difficult to electronically identify the in-plane magnetization state, since both the anisotropic magnetoresistance (AMR) and SMR have the twofold symmetry, which cannot be applied to distinguish the in-plane magnetization directions. Recently, an asymmetry magnetoresistance called unidirectional magnetoresistance (UMR) has been reported in FM/HM heterostructures [15], where the resistance changes by reversing the direction of either the magnetization or the applied current. Thus UMR could be utilized to detect magnetization directions with simple two-terminal geometry and can be applied in designing multistate memory devices [16]. In most studies on UMR, the FM layers are the Co film [15,17–19] or Co alloys [16,20]. To better understand the mechanisms of UMR and to further apply it in spintronic devices, it is necessary to explore the UMR in the FM/HM systems with the FM layer other than the Co-based materials. Apart from the FM/HM systems [15,17,18], UMR has been also discovered in ferromagnetic half metal/HM [21] and FM/topological insulator [20,22,23] systems.

So far, four mechanisms have been proposed to describe the UMR in the FM/HM systems: the spin accumulation induced by spin Hall effect (SHE) or Rashba effect [15,24], the electron-magnon scattering [18,25,26], the SOT effect [15,20], and the thermal effect [15,18,20,21], as indicated in Fig. 1. Due to the SHE in the HM layer or the Rashba effect at the FM/HM interface, the charge current will be converted to the spin current, which propagates along with the normal direction. Thus the spins will accumulate at the FM/HM interface with the polarization perpendicular to the current [15,24]. In the Fe/Pt system, the SHE in the Pt layer should provide the dominating contribution on the spin accumulation effect. Figure 1(a) indicates that such spin accumulation can form an artificial FM layer; then the opposite magnetization **M** will result in the different resistance for the spin polarization $\boldsymbol{\sigma}$ and **M** aligned parallelly or antiparallelly, which is similar to the current-in-plane giant magnetoresistance (CIP-GMR) in FM/normal metal/FM trilayers [27–29]. Both SHE and Rashba effect can generate the spin current flowing into the FM layer with $\boldsymbol{\sigma}$ perpendicular to the current. Such spin current also induces the creation or annihilation of magnons in the FM layer. As indicated in Fig. 1(b), the electron-magnon scattering process due to the spin current can change the resistance of the system, which also depends on the relative alignment between $\boldsymbol{\sigma}$ and **M** [25,30].

Besides the electron-magnon scattering, the SOT effect induced by the spin current, including the field like SOT (FL-SOT) and damping like SOT (DL-SOT), can cause the oscillation of **M** in the FM layer, while the oscillation amplitude depends on the relative orientation between $\boldsymbol{\sigma}$ and **M**, as shown in Fig. 1(c). Such oscillation of **M** can cause the variation of magnetoresistance [3,31,32], which induces UMR for the opposite current or magnetization directions. Figure 1(d) shows the thermal effect mechanism due to the strong current applied. While applying a strong current through the

*wuyizheng@fudan.edu.cn

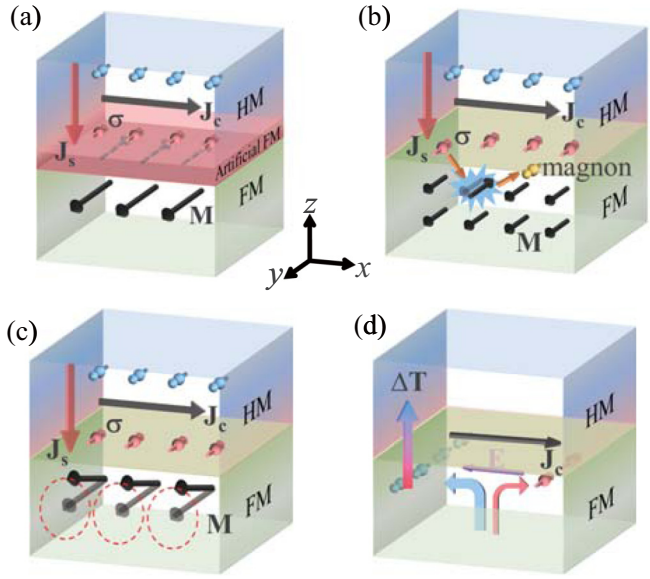

FIG. 1. Schematic diagrams of UMR mechanisms in FM/HM heterostructures: (a) the spin accumulation, (b) the electron-magnon scattering, (c) the SOT effect, and (d) the thermal effect. $\mathbf{J}_c$ is the current density by SHE, $\mathbf{J}_s$ is the induced spin current density by SHE or Rashba effect, $\mathbf{M}$ is the magnetization of the FM layer, $\boldsymbol{\sigma}$ is the orientation of the spin polarization, ΔT indicates the temperature gradient in the FM/HM heterostructure, and $\mathbf{E}$ is the additional electric field due to ANE.

heterostructure, a temperature gradient is likely generated along the normal direction due to the different thermal conductivities of the FM/HM heterostructure and the substrate. Then, the anomalous Nernst effect (ANE) will induce the additional voltage perpendicular to the in-plane magnetization direction [33,34]. To fully understand the UMR mechanisms in FM/HM systems, it is very crucial to separate all the contributions from different mechanisms. Note that the creation of magnons and the oscillation of $\mathbf{M}$ can be suppressed by a strong magnetic field [18,35]; thus the UMR induced by the electron-magnon scattering or the SOT effect should decay with the field strength. Meanwhile, the UMR induced by the spin accumulation or by the thermal effect should be independent of the field.

In this work, we investigated the UMR in single-crystalline Fe/Pt bilayers as a function of the temperature and the thickness of the Fe layer (t_{Fe}). An interesting sign reversal of UMR is found while increasing t_{Fe} at 10 K, and no sign reversal of UMR is observed at 300 K. The sign change of UMR also happens while increasing the temperature for the Fe film thicker than 1.6 nm. We experimentally extracted all the contributions from the four UMR mechanisms, including the spin accumulation (ξ_{spin}), the electron-magnon scattering (ξ_{magnon}), the thermal effect (ξ_{thermal}), and the fieldlike and dampinglike SOT (ξ_{FL} and ξ_{DL}), and found all these mechanisms coexist in the system. The extracted ξ_{thermal} is found to change its sign when increasing t_{Fe} due to the thickness-dependent Seebeck coefficient of Fe [36], and all the other UMR contributions keep the same sign with different temperatures and thicknesses. The competition between the thermal effect and other

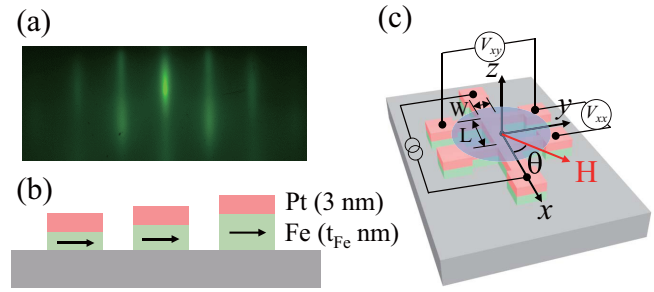

FIG. 2. (a) RHEED pattern of Fe(10 nm)/MgO(001) with the electron beam directed along MgO ⟨110⟩. (b) Illustration of the side view of the wedged sample. (c) Schematic illustration of Hall bar structure and measurement geometry.

mechanisms leads to the sign reversal of UMR in the Fe/Pt bilayers.

II. EXPERIMENT

Single crystalline Pt(3 nm)/Fe(t_{Fe} nm) heterostructures were fabricated on MgO(001) substrates by molecular beam epitaxy (MBE) in an ultrahigh vacuum (UHV) system with a base pressure of 2×10^{-10} Torr [37]. The MgO(001) single-crystal substrates were first prepared by annealing at 600 °C for 30 min in the UHV system. Then a 10-nm MgO was deposited as a seed layer by pulse laser deposition (PLD) at 300 °C to improve the surface quality. The Fe film was deposited by MBE at room temperature (RT) and then annealed at 300 °C for 10 min to improve the film quality. Figure 2(a) shows the typical reflection high-energy electron diffraction (RHEED) pattern of the Fe film, which indicates good epitaxial growth of Fe film. A 3-nm-thick Pt was deposited by PLD after the substrate was cooled down to RT. Before taking the sample out of the UHV chamber, we capped a 3-nm-thick MgO film to further protect the sample. The typical growth rate is ∼0.2 nm/min determined by a calibrated quartz thickness monitor.

In order to investigate the Fe-thickness-dependent properties, the Fe layer was grown into a wedge shape by moving the sample behind the shutter. The Fe thickness varies between 0 and 10 nm within the lateral distance of 5 mm. The wedge sample was then patterned into Hall bars with different thicknesses by standard ultraviolet lithography and an argon ion etching method. Figures 2(b) and 2(c) show the diagrammatic sketch of the sample for the magnetoresistance measurement. The Cr(10 nm)/Au(50 nm) electrodes were deposited by magnetron sputtering to make contact with the Hall bars. The width W of the Hall bar is 10 μm and the spacing L between two Hall bars is 30 μm. Note that all the Hall devices with different Fe thicknesses were prepared under the identical preparation condition, which can ensure a systematic thickness-dependent study.

We performed the UMR measurement utilizing the second harmonic method [31]. An ac current with the frequency of 13.7 Hz was injected into the longitudinal bar with an external field applied perpendicular to the current, and the first and second harmonic voltages were detected by the lock-in amplifiers. The UMR was determined by the second

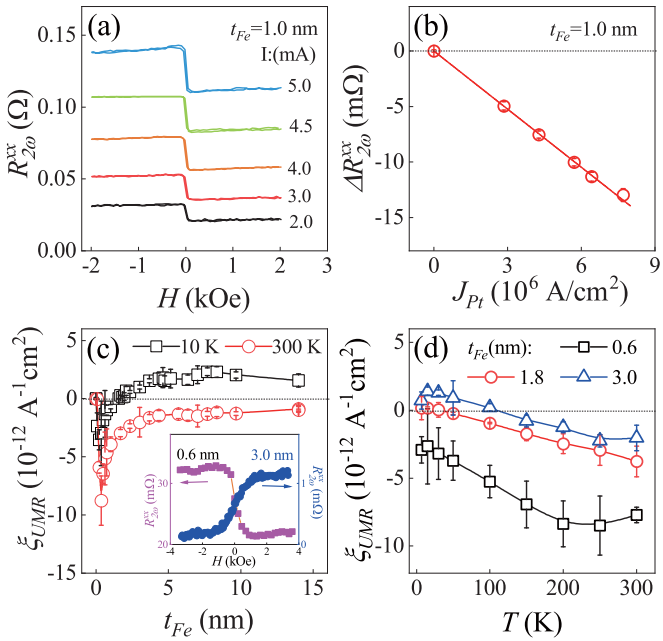

FIG. 3. (a) $R^{xx}_{2\omega} - H$ curves from the Fe(1 nm)/Pt sample measured with different currents at 300 K and (b) the extracted $\Delta R^{xx}_{2\omega}$ as a function of the current density J_{Pt} in the Pt layer from the Fe(1 nm)/Pt sample at 300 K. The solid line in (b) is the linear fitting. (c) The measured Fe-thickness-dependent $\xi_{\rm UMR}$ at 10 K and 300 K, respectively. The inset shows two representative $R^{xx}_{2\omega} - H$ curves with the opposite UMR sign. (d) Temperature-dependent $\xi_{\rm UMR}$ of the Fe(t_{Fe})/Pt bilayers with different t_{Fe}.

harmonic resistance ($R^{xx}_{2\omega}$) and the resistance was measured by the first harmonic voltages. The UMR from the wedge samples were measured at different temperatures on a cryogenic probe station (LakeShore EMPX-HF) with the maximum field of 0.6 T and a physical property measurement system (PPMS, Quantum Design) with the maximum field of 9 T.

III. RESULTS AND DISCUSSION

Figure 3(a) shows the measured $R^{xx}_{2\omega}$ as a function of H under different currents at 300 K for the Fe/Pt sample with $t_{Fe} = 1.0$ nm. All the data in Fig. 3 were measured in the cryogenic probe station. Apparently, the measured $R^{xx}_{2\omega}$ shows different values at positive ($+H$) and negative ($-H$) fields. The UMR is extracted by the difference of $R^{xx}_{2\omega}$ under $+H$ and $-H$, i.e., $\Delta R^{xx}_{2\omega} = R^{xx}_{2\omega,+H} - R^{xx}_{2\omega,-H}$. We further demonstrate that $\Delta R^{xx}_{2\omega}$ is linearly proportional to the current density J_{Pt} in the Pt layer [15,17], as shown in Fig. 3(b). Here, J_{Pt} is determined by $J_{Pt} = I_{\rm tot} R_{\rm tot}/(W R_{Pt} t_{Pt})$. $I_{\rm tot}$, $R_{\rm tot}$, R_{Pt}, and t_{Pt} are the applied current, the measured resistance of Fe/Pt bilayer, the resistance of single Pt layer, and the thickness of Pt layer, respectively. We further determined UMR with $\xi_{\rm UMR} = \Delta R^{xx}_{2\omega}/(R_{\rm tot} J_{Pt})$, which represents the resistance ratio of UMR under a unit current density [15–18,20]. Figure 3(c) plots the measured t_{Fe}-dependent $\xi_{\rm UMR}$ at 10 K and 300 K. The amplitude of $\xi_{\rm UMR}$ increases sharply with a maximum at $t_{Fe} \sim 0.3$ nm, and then gradually decreases to a constant while increasing t_{Fe}. The sharp enhancement at $t_{Fe} \sim 0.3$ nm can be attributed to the establishment of Fe ferromagnetism in the Fe thin film [38,39]. Using the *ex situ* atomic force microscope, we also investigated the thickness-dependent roughness of Fe film from a wedged Fe sample, and found the roughness of the Fe surface has no obvious change at $t_{Fe} \sim 0.3$ nm; thus the observed sharp change of UMR at $t_{Fe} \sim 0.3$ nm is unlikely related to the change of the interface roughness.

The t_{Fe}-dependent $\xi_{\rm UMR}$ varies from negative to positive at 10 K, while it remains negative at 300 K. The inset of Fig. 3(c) shows two $R^{xx}_{2\omega} - H$ curves from the Fe(0.6 nm)/Pt and Fe(3.0 nm)/Pt bilayers, which demonstrated the opposite polarity of UMR. Figure 3(d) displays the temperature dependence of $\xi_{\rm UMR}$ for the Fe/Pt bilayers with $t_{Fe} = 0.6$, 1.8, and 3.0 nm, respectively. $\xi_{\rm UMR}$ of all samples varies monotonically with the temperature and a sign reversal can be found at about 100 K for the Fe(3 nm)/Pt bilayer.

In previous studies on the UMR in metallic FM/HM systems [15–20], no sign reversal has been reported by varying temperature or film thickness. The sign of UMR can be tuned by replacing the HM layer with the opposite spin Hall angle [15]. In GaMnAs/BiSb heterostructure, Khang *et al*. reported the switch of UMR polarity as a function of current density [23], which was interpreted as the competition between the bulk spin-dependent scattering mechanism and the magnon scattering mechanism. In the Fe/Pt system, we found that the measured $\Delta R^{xx}_{2\omega}$ always changes linearly with J_{Pt}, so the observed sign reversal of UMR is independent of the current density. In order to understand the origin of the thickness- and temperature-dependent sign reversal of UMR, it is necessary to separate the contributions from all four UMR mechanisms under different conditions.

Since both the electron-magnon scattering and SOT effects can be suppressed by a large magnetic field, while both the spin accumulation and the thermal effect contributions are independent of field [15,18], we further perform the UMR measurement with the field up to 6 T. Figures 4(a) and 4(b) show the normalized $R^{xx}_{2\omega} - H$ curves for different t_{Fe} under similar J_{Pt} at 10 K and 300 K, respectively. $R^{xx}_{2\omega}$ is almost saturated under 6 T, and the $R^{xx}_{2\omega} - H$ curve reverses the polarity with the increasing t_{Fe} at 10 K, while only the same polarity of $R^{xx}_{2\omega}$ at different t_{Fe} can be observed at 300 K. $\Delta R^{xx}_{2\omega}$ at $H = 6$ T can be extracted from $R^{xx}_{2\omega} - H$ curves, and Figs. 4(c) and 4(d) show the determined $\Delta R^{xx}_{2\omega}$ as a function of J_{Pt} for different t_{Fe} at 10 K and 300 K, respectively. $\Delta R^{xx}_{2\omega}$ changes linearly with J_{Pt}, in good agreement with the results measured in the probe station. Figure 4(c) shows the slope at 10 K changes from negative to positive while increasing t_{Fe}, indicating the t_{Fe}-dependent sign reversal of $\xi_{\rm UMR}$. At 300 K, $\xi_{\rm UMR}$ is always negative for all the Fe/Pt samples with different t_{Fe}. Moreover, we also demonstrate that the measurement on the single Pt layer gives zero $\Delta R^{xx}_{2\omega}$, which indicates the indispensability of the FM layer for the observed UMR in Fe/Pt bilayers.

We further separate the UMR contributions from the four different mechanisms to understand the origin of the sign reversal of UMR. As indicated in Fig. 4(b), $|R^{xx}_{2\omega}|$ has a quick decrease for $H < 1.5$ T, then gradually decreases for the stronger H. $|R^{xx}_{2\omega}|$ is almost saturated at 6 T. The quick decrease of $|R^{xx}_{2\omega}|$ for the weak field can be attributed to the suppression of magnons by magnetic field [15,18], and the slow decrease of $|R^{xx}_{2\omega}|$ at larger field range is due to the field suppression of the FL-SOT effect [18]. Finally, the saturation signal of $|R^{xx}_{2\omega}|$ is related to the contribution from the thermal

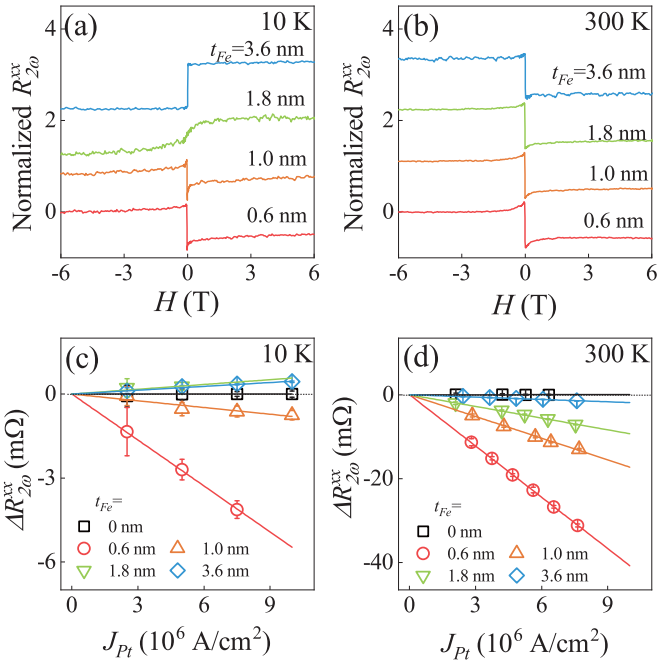

FIG. 4. Normalized $R^{xx}_{2\omega}$ versus H curves for different Fe thicknesses at (a) 10 K and (b) 300 K. The extracted $\Delta R^{xx}_{2\omega}$ as a function of J_{Pt} for different t_{Fe} at (c) 10 K and (d) 300 K, respectively. The solid lines in (c) and (d) are the linear fitting of the measured data. All the results are measured by PPMS.

effect and the spin accumulation. Thus the UMR contributions from the electron-magnon scattering of the SOT effect, i.e., $R^{xx}_{2\omega,\ \mathrm{magnon}+FL}$, can be obtained by measuring the difference of $R^{xx}_{2\omega}$ at 6 T and at ∼0 T. However, $R^{xx}_{2\omega,\ \mathrm{magnon}+FL}$ does not contribute to the sign reversal of UMR, while Fig. 4 clearly shows that the UMR at 6 T changes its sign with different t_{Fe}.

In order to identify the UMR contributions from the SOT effect, the thermal effect, and the spin accumulation, we further perform the angular dependent measurement of $R^{xx}_{2\omega}$ and $R^{xy}_{2\omega}$ with the rotation field stronger than 1.5 T. According to the results in Fig. 4, the UMR contribution from the electron-magnon scattering can be ignored. Thus the angular dependent $R^{xx}_{2\omega}$ and $R^{xy}_{2\omega}$ can be written as [15]

$$R^{xx}_{2\omega} = R^{xx}_{2\omega,\ FL}\sin 2\theta\ \cos\theta + \left(R^{xx}_{2\omega,\ Th} + R^{xx}_{2\omega,\ spin}\right)\sin\theta, \quad (1)$$

$$R^{xy}_{2\omega} = R^{xy}_{2\omega,\ FL}(2\cos^3\theta - \cos\theta) + \left(R^{xy}_{2\omega,\ Th} + R^{xy}_{2\omega,\ DL}\right)\cos\theta, \quad (2)$$

where $R^{xx}_{2\omega,\ FL}$, $R^{xx}_{2\omega,\ Th}$, and $R^{xx}_{2\omega,\ \mathrm{spin}}$ represent the contributions on $R^{xx}_{2\omega}$ from the FL-SOT effect, the thermal effect, and the spin accumulation, while $R^{xy}_{2\omega,\ FL}$, $R^{xy}_{2\omega,\ DL}$, and $R^{xy}_{2\omega,\ Th}$ represent the FL-SOT, the DL-SOT, and the thermal contributions to $R^{xy}_{2\omega}$, respectively. θ is the angle between the magnetic moment **M** and the current, which is expected to be the same as the field angle for $H > 1.5$ T. So, $R^{xx}_{2\omega,\ FL}$, $R^{xx}_{2\omega,\ Th} + R^{xx}_{2\omega,\ \mathrm{spin}}$, $R^{xy}_{2\omega,\ FL}$, and $R^{xy}_{2\omega,\ Th} + R^{xy}_{2\omega,\ DL}$ can be determined by the θ-dependent measurements. Moreover, it is well known that the SOT contribution $R^{xy}_{2\omega,\ DL}$ can be fully suppressed under a strong field. Thus the thermal contribution $R^{xy}_{2\omega,\ Th}$ can be determined by a strong field. Since the thermal signal is proportional to the measuring distance [15], the thermal contributions $R^{xx}_{2\omega,\ Th}$ can be obtained by the relation of $R^{xx}_{2\omega,\ Th} = L/W R^{xy}_{2\omega,\ Th}$, with L and W as the length and width of the Hall bar. Then, the contributions $R^{xx}_{2\omega,\ Th}$ and $R^{xx}_{2\omega,\ \mathrm{spin}}$ can be fully separated and the sign reversal of UMR at strong field can be further understood.

Figures 5(a) and 5(b) show the θ-dependent $R^{xx}_{2\omega}$ at 10 K and 300 K for the Fe/Pt samples with $t_{Fe} = 0.6$ nm and 1.8 nm, respectively. The applied field H is 6 T, which can align **M** with **H**. The solid lines in Figs. 5(a) and 5(b) are the fitting curves with a simple $\sin\theta$ dependence. Our analysis indicates that the effect of FL-SOT on UMR is negligible at the field of 6 T. Then, Eq. (1) can be simplified to $R^{xx}_{2\omega} \approx (R^{xx}_{2\omega,\ Th} + R^{xx}_{2\omega,\ \mathrm{spin}})\sin\theta$. Figures 5(c) and 5(d) show the θ-dependent $R^{xy}_{2\omega}$ at 10 K and 300 K for the Fe/Pt samples with $t_{Fe} = 0.6$ nm and 1.8 nm, respectively. Due to the negligible FL-SOT component under 6 T, Eq. (2) can be simplified to $R^{xy}_{2\omega} \approx (R^{xy}_{2\omega,\ Th} + R^{xy}_{2\omega,\ DL})\cos\theta$. The amplitude of $R^{xy}_{2\omega,\ Th} + R^{xy}_{2\omega,\ DL}$ can be extracted by fitting the $R^{xy}_{2\omega}$-θ curves with a $\cos\theta$ dependence, as shown by the solid lines in Figs. 5(c) and 5(d). The good agreement between the fitting curves and measured data further proves that the FL-SOT component is negligible under a large field.

Figures 5(b) and 5(d) show that both θ-dependent curves of $R^{xx}_{2\omega}$ and $R^{xy}_{2\omega}$ contain the opposite θ dependence at 10 K and 300 K for $t_{Fe} = 1.8$ nm, which is consistent with the field-dependent measurements in Fig. 4. In order to determine the contributions on UMR from the thermal effect and the spin accumulation, we need to separate the SOT contribution $R^{xy}_{2\omega,\ DL}$. Thus we further measure the field-dependent $R^{xy}_{2\omega}$ for the Fe/Pt sample with $t_{Fe} = 0.6$ nm and 1.8 nm, as shown in Figs. 5(e) and 5(f). The sign reversal of $R^{xy}_{2\omega}$ also occurs at 10 K and 300 K for the sample with $t_{Fe} = 1.8$ nm in Fig. 5(f). In contrast with the field-dependent measurement of $R^{xx}_{2\omega}$ in Fig. 4, $R^{xy}_{2\omega}$ decreases with H, but does not saturate even at 6 T. This indicates that the effect of FL-SOT on UMR is much smaller than that of DL-SOT, since the DL-SOT effect $R^{xy}_{2\omega,\ DL}$ only contributes to the $R^{xy}_{2\omega}$ measurement. In Ref. [20], Lv *et al*. reported that $R^{xy}_{2\omega,\ DL}$ is inversely proportional to $H + H_{eff}$. Here, H_{eff} is the effective out-of-plane anisotropic field and can be determined as the saturation field while applying the field normal to the film. By measuring the out-of-plane hysteresis loop utilizing anomalous Hall effect (AHE), we can determine the value of H_{eff} for the Fe(t_{Fe})/Pt bilayers at different temperatures. Figures 5(g) and 5(h) indicate that $R^{xy}_{2\omega}$ shows a good linear dependence on $(H + H^{eff}_k)^{-1}$ for $H > 1.5$ T. The contribution of the thermal effect on $R^{xy}_{2\omega}$ should be independent of H; thus $R^{xy}_{2\omega,\ Th}$ can be determined as the intercept through the linear fitting. Then, the longitudinal UMR $R^{xx}_{2\omega,\ Th}$ due to the thermal effect can be determined through the geometric transformation. In Figs. 5(g) and 5(h), we also plot the measured $R^{xy}_{2\omega}$ through the θ-dependent measurements with different H, which are consistent with the results measured by sweeping the field perpendicular to the current. After $R^{xx}_{2\omega,\ Th}$ is determined, we can further quantify the $R^{xx}_{2\omega,\ \mathrm{spin}}$ due to the spin accumulation from $R^{xx}_{2\omega}$ at 6 T.

Through the foregoing analysis, we can determine the UMR contributions $R^{xx}_{2\omega,\ Th}$ and $R^{xx}_{2\omega,\ \mathrm{spin}}$ measured at 6 T, and $R^{xx}_{2\omega,\ \mathrm{magnon}+FL}$ by calculating the difference between the UMR values at ∼0 T and 6 T. We performed the systematical

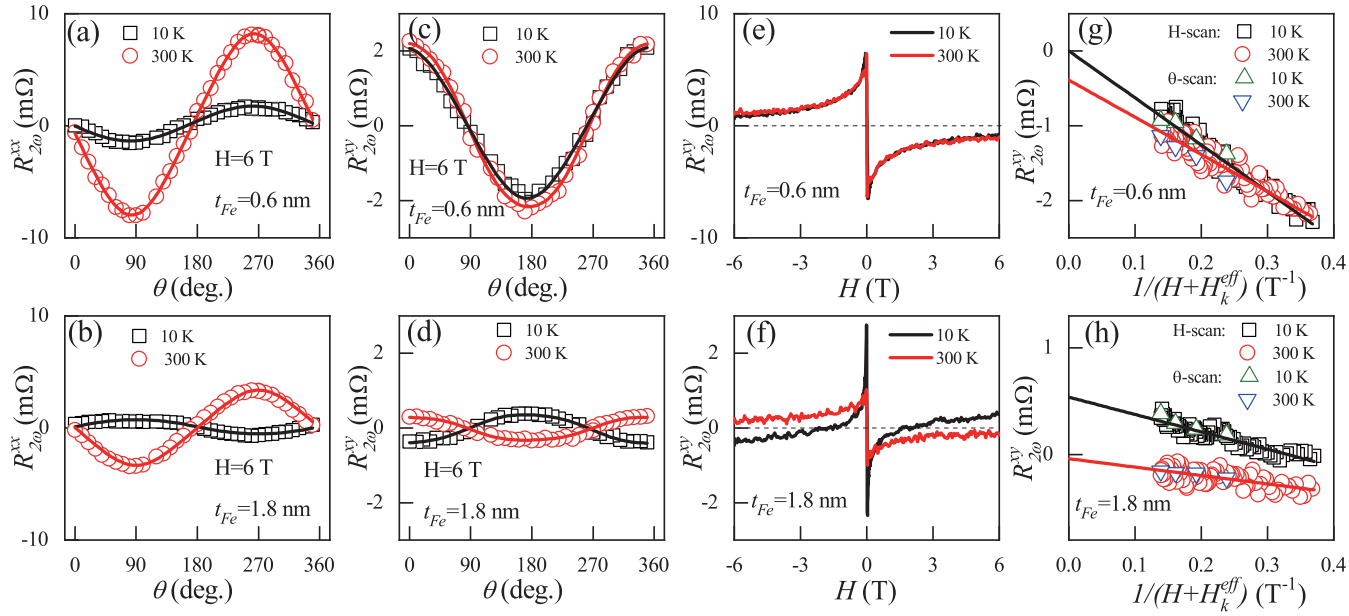

FIG. 5. (a),(b) Angular dependence of $R^{xx}_{2\omega}$ at 10 K and 300 K for (a) $t_{Fe} = 0.6$ nm and (b) $t_{Fe} = 1.8$ nm, respectively. The solid lines are the fitting curves according to the $\sin\theta$ dependence. (c),(d) Angular dependence of $R^{xy}_{2\omega}$ for (c) $t_{Fe} = 0.6$ nm and (d) $t_{Fe} = 1.8$ nm, respectively. The solid lines are the fitting curves with the $\cos\theta$ dependence. (e),(f) Field dependence of $R^{xy}_{2\omega}$ for (e) $t_{Fe} = 0.6$ nm and (f) $t_{Fe} = 1.8$ nm with the field H applied perpendicular to the current. (g),(h) The measured $R^{xy}_{2\omega}$ as a function of $(H + H_k^{eff})^{-1}$ for (g) $t_{Fe} = 0.6$ nm and (h) $t_{Fe} = 1.8$ nm. The solid lines in (g) and (h) are the linear fits to the data and the intercept of the fitted line represents the contribution of the thermal effect. The green up triangles and blue down triangles represent the $R^{xy}_{2\omega}$ data obtained from the $R^{xy}_{2\omega} - \theta$ curves under different H. The circles and squares are the measured $R^{xy}_{2\omega}$ from the $R^{xy}_{2\omega} - H$ curves in (e) and (f) for $H > 1.5$ T.

measurements with different t_{Fe} at different temperatures. The current in the Pt layer should vary with the Fe thickness, so, in the later discussion, we focus on $\xi_{\text{magnon}+FL}$, ξ_{thermal}, and ξ_{spin}, which are the UMR ratios per J_{Pt} from different mechanisms. Figures 6(a) and 6(b) show the thickness dependence of $\xi_{\text{magnon}+FL}$, ξ_{thermal}, and ξ_{spin} at 10 K and 300 K, respectively. It should be noted that $\xi_{\text{magnon}+FL}$ here reflects the total contribution from the magnon and FL-SOT components at low field, and is irrelevant to the sign reversal of UMR at 6 T. Both $\xi_{\text{magnon}+FL}$ and ξ_{spin} have negative sign, and the magnitudes of both $\xi_{\text{magnon}+FL}$ and ξ_{spin} decrease with t_{Fe} at 10 K and 300 K due to the interfacial origin of these two contributions. Moreover, our results show that ξ_{thermal} has a distinct sign reversal from negative to positive while increasing t_{Fe}, and the transition thickness t^{tr}_{Fe} is ∼0.7 nm at 10 K and ∼2.6 nm at 300 K, which is indicated by the red arrows in Fig. 6. We also separate all the contributions on UMR at the different temperatures for the Fe/Pt sample with $t_{Fe} = 1.8$ nm. Figure 6(c) shows that ξ_{thermal} varies from positive to negative at a transition temperature of ∼200 K. In Fig. 6(d), we further plot the transition thickness t^{tr}_{Fe} of ξ_{thermal} measured at different temperatures, which increases with the temperature. Due to the competition between ξ_{thermal} and ξ_{spin}, the total UMR ξ_{UMR} at 6 T also presents the sign reversal from negative to positive at a transition thickness, which is much smaller than that of ξ_{thermal}. As shown in Fig. 6(d), ξ_{UMR} should present a sign reversal as a function of temperature for the Fe/Pt sample with $t_{Fe} > 1.6$ nm, and also contain a thickness-dependent sign change if measured at the temperature less than 100 K, which is consistent with the results in Figs. 3(c) and 3(d).

In Fig. 6(c), the magnitude of $\xi_{\text{magnon}+FL}$ increases with the temperature, and this can be understood by the electron-magnon scattering mechanism, which may increase with the magnon density at higher temperature. Figures 6(a)–6(c) also indicate that the magnitude of ξ_{spin} increases with the temperature. For the Fe(1.8 nm)/Pt sample, ξ_{spin} at 300 K is ∼15 times stronger than that at 10 K. Usually, the UMR contribution due to the spin accumulation mechanism scales with the spin Hall angle and the spin-diffusion length in the HM layer [15,24]. But the spin Hall angle is nearly independent of the temperature [40,41], and the spin-diffusion length in the Pt layer decreases slightly with the temperature [37,40]; thus such strong enhancement of ξ_{spin} with the temperature is hard to explain by the change of the spin Hall angle or the spin-diffusion length. ξ_{spin} in the Fe/Pt bilayer may strongly depend on the electronic structures at the Fe/Pt interface and in the Fe film. As Zhang *et al*. [24] pointed out, the UMR in the FM/HM bilayer also strongly depends on the difference between the spin polarizations of conductivity and density of states at Fermi energy, which may contain strong temperature effect. The fact that UMR due to the spin-accumulation mechanism increases with the temperature may benefit the spintronic device applications, because the other well-known magnetoresistance effects, such as GMR [27] or tunneling magnetoresistance (TMR) [42], always decrease with the temperature.

The sign change of ξ_{thermal} should attribute to the ANE effect in Fe film and the ANE signal is usually proportional to the Seebeck coefficient S_{xx}. Chuang *et al*. [36] recently reported that the ANE signal and S_{xx} in Fe films can change the sign at $t_{Fe} \sim 6$ nm at room temperature. The sign change

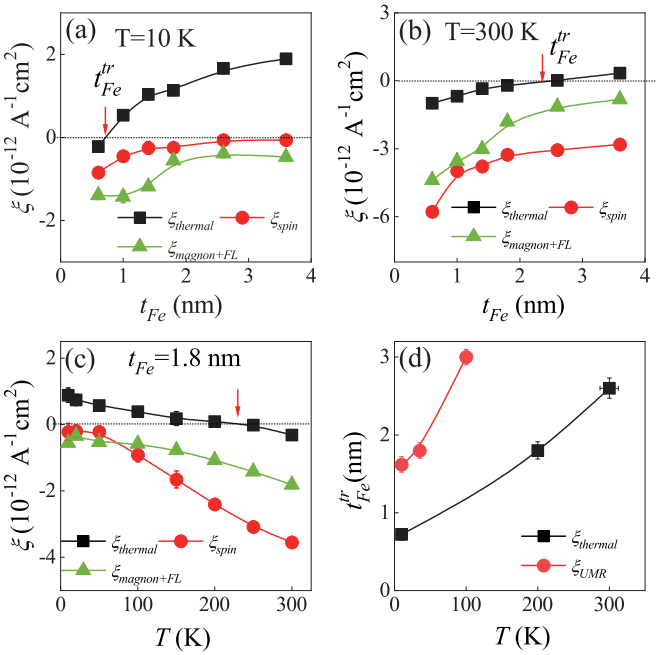

FIG. 6. Thickness dependent $\xi_{\text{magnon}+FL}$, ξ_{thermal}, and ξ_{spin} measured at (a) 10 K and (b) 300 K, respectively. (c) Temperature dependence of $\xi_{\text{magnon}+FL}$, ξ_{thermal}, and ξ_{spin} for $t_{Fe} = 1.8$ nm. (d) Plot of the critical thickness of the sign reversal of ξ_{thermal} and ξ_{UMR} as a function of temperature. The solid lines serve a guide to the eye and the red arrows in (a)–(c) indicate the sign reversal of ξ_{thermal}.

of S_{xx} can be described by the mean free path model $S(t) = S_g(1 - b/t)$ [36,43]. Here, S_g is the bulk Seebeck coefficient, t is the film thickness, and b is the parameter related to the surface and grain-boundary scattering. When t is comparable with the mean free path of carriers, S_{xx} will be significantly influenced by the surface scattering. Our results in Fig. 6(d) indicate that the parameter b may be smaller at low temperature; thus the transition thickness t_{Fe}^{tr} increases with the temperature. Note that no temperature or thickness dependent sign change of UMR has been reported in other metallic FM/HM systems before, since Chuang reported that all the Co, Ni, and Py($Ni_{80}Fe_{20}$) films do not show the sign change of ANE and S_{xx} [36].

IV. CONCLUSION

The UMR in single-crystalline Fe/Pt bilayers has been systematically investigated as a function of Fe thickness t_{Fe} at different temperatures. An interesting thickness-dependent sign reversal is observed at low temperature, while no sign reversal of UMR is observed at high temperature, which has never been reported in other systems. Moreover, the Fe/Pt bilayers present the interesting temperature-dependent sign reversal of UMR for $t_{Fe} > 1.6$ nm. By performing the field-dependent measurements, and comparing the longitudinal and transverse UMR signals, the major contributions of $\xi_{\text{magnon}+FL}$, ξ_{thermal}, and ξ_{spin} are quantitatively separated, and the sign reversal of UMR is attributed to ξ_{thermal} due to the thermal effect. Our results further emphasize the importance of the thermal contribution to UMR in ferromagnet/heavy metal heterostructures, which not only promote the understanding of UMR, but also provide the potential application in information reading devices.

ACKNOWLEDGMENTS

We gratefully acknowledge useful discussions with Professor W. Zhang and Professor S. S.-L. Zhang. This work was supported by the National Natural Science Foundation of China (Grants No. 11974079, No. 11734006, and No. 12104302), National Key Research and Development Program of China (Grant No. 2016YFA0300703), the Shanghai Municipal Science and Technology Major Project (Grant No. 2019SHZDZX01), and China Postdoctoral Science Foundation (Grant No. 2018M630395).

[1] Y. Kajiwara, K. Harii, S. Takahashi, J. Ohe, K. Uchida, M. Mizuguchi, H. Umezawa, H. Kawai, K. Ando, K. Takanashi, S. Maekawa, and E. Saitoh, Nature (London) **464**, 262 (2010).

[2] I. M. Miron, K. Garello, G. Gaudin, P.-J. Zermatten, M. V. Costache, S. Auffret, S. Bandiera, B. Rodmacq, A. Schuhl, and P. Gambardella, Nature (London) **476**, 189 (2011).

[3] L. Liu, C.-F. Pai, Y. Li, H. W. Tseng, D. C. Ralph, and R. A. Buhrman, Science **336**, 555 (2012).

[4] S. Y. Huang, X. Fan, D. Qu, Y. P. Chen, W. G. Wang, J. Wu, T. Y. Chen, J. Q. Xiao, and C. L. Chien, Phys. Rev. Lett. **109**, 107204 (2012).

[5] H. Nakayama, M. Althammer, Y. T. Chen, K. Uchida, Y. Kajiwara, D. Kikuchi, T. Ohtani, S. Geprags, M. Opel, S. Takahashi, R. Gross, G. E. W. Bauer, S. T. B. Goennenwein, and E. Saitoh, Phys. Rev. Lett. **110**, 206601 (2013).

[6] K. Ando, S. Takahashi, J. Ieda, H. Kurebayashi, T. Trypiniotis, C. H. W. Barnes, S. Maekawa, and E. Saitoh, Nat. Mater. **10**, 655 (2011).

[7] W. Zhang, W. Han, X. Jiang, S.-H. Yang, and S. S. P. Parkin, Nat. Phys. **11**, 496 (2015).

[8] H. L. Wang, C. H. Du, Y. Pu, R. Adur, P. C. Hammel, and F. Y. Yang, Phys. Rev. B **88**, 100406(R) (2013).

[9] K. Uchida, S. Takahashi, K. Harii, J. Ieda, W. Koshibae, K. Ando, S. Maekawa, and E. Saitoh, Nature (London) **455**, 778 (2008).

[10] D. Qu, S. Y. Huang, J. Hu, R. Wu, and C. L. Chien, Phys. Rev. Lett. **110**, 067206 (2013).

[11] E. B. Myers, D. C. Ralph, J. A. Katine, R. N. Louie, and R. A. Buhrman, Science **285**, 867 (1999).

[12] D. C. Ralph and M. D. Stiles, J. Magn. Magn. Mater. **320**, 1190 (2008).

[13] J. Kim, P. Sheng, S. Takahashi, S. Mitani, and M. Hayashi, Phys. Rev. Lett. **116**, 097201 (2016).

[14] X. Zhou, L. Ma, Z. Shi, W. J. Fan, J.-G. Zheng, R. F. L. Evans, and S. M. Zhou, Phys. Rev. B **92**, 060402(R) (2015).

[15] C. O. Avci, K. Garello, A. Ghosh, M. Gabureac, S. F. Alvarado, and P. Gambardella, Nat. Phys. **11**, 570 (2015).

[16] C. O. Avci, M. Mann, A. J. Tan, P. Gambardella, and G. S. D. Beach, Appl. Phys. Lett. **110**, 203506 (2017).
[17] Y. Yin, D.-S. Han, M. C. H. d. Jong, R. Lavrijsen, R. A. Duine, H. J. M. Swagten, and B. Koopmans, Appl. Phys. Lett. **111**, 232405 (2017).
[18] C. O. Avci, J. Mendil, G. S. D. Beach, and P. Gambardella, Phys. Rev. Lett. **121**, 087207 (2018).
[19] K. Hasegawa, T. Koyama, and D. Chiba, Phys. Rev. B **103**, L020411 (2021).
[20] Y. Lv, J. Kally, D. Zhang, J. S. Lee, M. Jamali, N. Samarth, and J.-P. Wang, Nat. Commun. **9**, 111 (2018).
[21] C. Lidig, J. Cramer, L. Weißhoff, T. R. Thomas, T. Kessler, M. Kläui, and M. Jourdan, Phys. Rev. Appl. **11**, 044039 (2019).
[22] K. Yasuda, A. Tsukazaki, R. Yoshimi, K. S. Takahashi, M. Kawasaki, and Y. Tokura, Phys. Rev. Lett. **117**, 127202 (2016).
[23] N. H. Duy Khang and P. N. Hai, J. Appl. Phys. **126**, 233903 (2019).
[24] S. S.-L. Zhang and G. Vignale, Phys. Rev. B **94**, 140411(R) (2016).
[25] S. Langenfeld, V. Tshitoyan, Z. Fang, A. Wells, T. A. Moore, and A. J. Ferguson, Appl. Phys. Lett. **108**, 192402 (2016).
[26] W. P. Sterk, D. Peerlings, and R. A. Duine, Phys. Rev. B **99**, 064438 (2019).
[27] M. N. Baibich, J. M. Broto, A. Fert, F. Nguyen Van Dau, F. Petroff, P. Etienne, G. Creuzet, A. Friederich, and J. Chazelas, Phys. Rev. Lett. **61**, 2472 (1988).
[28] R. E. Camley and J. Barnaś, Phys. Rev. Lett. **63**, 664 (1989).
[29] P. M. Levy, S. Zhang, and A. Fert, Phys. Rev. Lett. **65**, 1643 (1990).
[30] T. Li, S. Kim, S.-J. Lee, S.-W. Lee, T. Koyama, D. Chiba, T. Moriyama, K.-J. Lee, K.-J. Kim, and T. Ono, Appl. Phys. Express **10**, 073001 (2017).
[31] J. Kim, J. Sinha, M. Hayashi, M. Yamanouchi, S. Fukami, T. Suzuki, S. Mitani, and H. Ohno, Nat. Mater. **12**, 240 (2013).
[32] K. Garello, I. M. Miron, C. O. Avci, F. Freimuth, Y. Mokrousov, S. Blugel, S. Auffret, O. Boulle, G. Gaudin, and P. Gambardella, Nat. Nanotechnol. **8**, 587 (2013).
[33] M. Mizuguchi, S. Ohata, K.-i. Uchida, E. Saitoh, and K. Takanashi, Appl. Phys. Express **5**, 093002 (2012).
[34] C. O. Avci, K. Garello, M. Gabureac, A. Ghosh, A. Fuhrer, S. F. Alvarado, and P. Gambardella, Phys. Rev. B **90**, 224427 (2014).
[35] B. Raquet, M. Viret, E. Sondergard, O. Cespedes, and R. Mamy, Phys. Rev. B **66**, 024433 (2002).
[36] T. C. Chuang, P. L. Su, P. H. Wu, and S. Y. Huang, Phys. Rev. B **96**, 174406 (2017).
[37] J. X. Li, M. W. Jia, Z. Ding, J. H. Liang, Y. M. Luo, and Y. Z. Wu, Phys. Rev. B **90**, 214415 (2014).
[38] C. Martínez Boubeta, C. Clavero, J. M. García-Martín, G. Armelles, A. Cebollada, L. Balcells, J. L. Menéndez, F. Peiró, A. Cornet, and M. F. Toney, Phys. Rev. B **71**, 014407 (2005).
[39] S. Yang, H. K. Park, J. S. Kim, J. Y. Kim, and B. G. Park, J. Appl. Phys. **110**, 093920 (2011).
[40] M. Isasa, E. Villamor, L. E. Hueso, M. Gradhand, and F. Casanova, Phys. Rev. B **91**, 024402 (2015).
[41] K. Nakagawara, S. Kasai, J. Ryu, S. Mitani, L. Liu, M. Kohda, and J. Nitta, Appl. Phys. Lett. **115**, 162403 (2019).
[42] J. S. Moodera, L. R. Kinder, T. M. Wong, and R. Meservey, Phys. Rev. Lett. **74**, 3273 (1995).
[43] Y.-J. Chen and S.-Y. Huang, Phys. Rev. Lett. **117**, 247201 (2016).